Journal of Materials Chemistry B

ROYAL SOCIETY OF CHEMISTRY

PAPER

View Article Online
View Journal | View Issue

Cite this: J. Mater. Chem. B, 2024, 12, 2373

Jellyfish-inspired smart tetraphenylethene lipids with unique AIE fluorescence, thermal response, and cell membrane interaction†

Yujie Zheng,‡[ac] Yu Li,‡[a] Changsheng Ke,‡[ac] Mojie Duan,[a] Lijun Zhu,[a] Xin Zhou,[abd] Minghui Yang,[a] Zhong-Xing Jiang *[ab] and Shizhen Chen*[abd]

Smart lipids with fluorescence emission, thermal response, and polyethylene glycolation (PEGylation) functions can be highly valuable for formulation, image-traceable delivery, and targeted release of payloads. Herein, a series of jellyfish-shaped amphiphiles with a tetraphenylethene (TPE) core and four symmetrical amphiphilic side chains were conveniently synthesized and systematically investigated as smart lipids. Compared with regular amphiphilic TPE lipids and phospholipids, the unprecedented jellyfish-shaped molecular geometry was found to enable a series of valuable capabilities, including sensitive and responsive aggregation-induced emission of fluorescence (AIE FL) and real-time FL monitoring of drug uptake. Furthermore, the jellyfish-shaped geometry facilitated the concentration-dependent aggregation from unimolecular micelles at low concentrations to "side-by-side" spherical aggregates at high concentrations and a unique mode of AIE. In addition, the size and the arrangement of the amphiphilic side chains were found to dominate the aggregate stability, cell uptake, and thus the cytotoxicity of the amphiphiles. This study has unprecedentedly developed versatile smart TPE lipids with precise structures, and unique physicochemical and biological properties while the peculiar structure–property relationship may shed new light on the design and application of AIE fluorophores and functional lipids in biomedicine and materials science.

Received 5th September 2023,
Accepted 26th January 2024

DOI: 10.1039/d3tb02068a

rsc.li/materials-b

Introduction

In recent years, lipid-based nanoparticles (LNPs) have achieved tremendous success in the delivery of various small molecule drugs, peptides, proteins, nucleic acids, *etc.*[1] Since the first LNP drug, Doxil®, was approved in 1995, the recent approval of SARS-COVID-2-mRNA vaccines has set another milestone.[2] The rapid development of LNPs creates an urgent demand for novel smart lipids, such as fluorescent lipids, stimulus-responsive lipids, ionizable cationic lipids, *etc.*[3] Among various lipids, polyethylene glycolated (PEGylated) lipids, such as DSPE-PEG_{2000}, have attracted considerable attention as the 2nd generation lipids that can reduce immunogenicity and dosing frequency, thus optimizing pharmacokinetics.[4] However, the polydispersity of polyethylene glycols (PEGs) adversely complicates the purification, quality control, and drug regulatory approval.[5] Fortunately, all these issues can be addressed by replacing regular PEGs with monodisperse PEGs (M-PEGs),[6] which provide M-PEGylated lipids with a single component instead of a polymeric mixture. In particular, branched PEGs usually exhibit superior efficacy in optimizing the pharmacokinetics of LNPs compared to their linear counterparts,[7] which encourages the substitution of linear long PEGs with branched short PEGs. In addition, branched short M-PEG-based biomaterials can have sharp and precisely tunable lower critical solution temperatures (LCSTs),[8] facilitating the local temperature-triggered release of the payload from PEGylated LNPs for targeted therapy.[8c] Therefore, the development of branched M-PEG-based smart lipids can provide high-performance LNPs with precise ingredients, superior pharmacokinetics, and thermal responsiveness.

The integration of a fluorophore into lipids, *i.e.* fluorescent lipids, can facilitate the real-time monitoring of the delivery,

[a] State Key Laboratory of Magnetic Resonance and Atomic and Molecular Physics, National Center for Magnetic Resonance in Wuhan, Wuhan Institute of Physics and Mathematics, Innovation Academy for Precision Measurement Science and Technology, Chinese Academy of Sciences-Wuhan National Laboratory for Optoelectronics, Wuhan 430071, China. E-mail: zxjiang@apm.ac.cn, chenshizhen@apm.ac.cn
[b] University of Chinese Academy of Sciences, Beijing 100049, China
[c] School of Pharmaceutical Sciences, Wuhan University, Wuhan 430071, China
[d] Optics Valley Laboratory, Wuhan 430074, China

† Electronic supplementary information (ESI) available: Synthesis and characterization of intermediates, measurement of Log *P*, FL quantum yield, formulation, DLS and TEM of nanoparticles, cytotoxicity assay, hemolysis test, molecular dynamics simulations, supplementary figures and tables, and copies of $^{1}H/^{13}C$ NMR and MS spectra. See DOI: https://doi.org/10.1039/d3tb02068a

‡ These authors contributed equally to this work.

uptake, and degradation processes of LNPs,[3a] which is a research hotspot and a cornerstone for the development of LNP drugs.[10] TPE represents a classic fluorophore with aggregation-induced emission of fluorescence.[9] Since lipid aggregation is prevalent in the life cycle of LNPs, TPE could be a valuable fluorescent scaffold for smart lipids to monitor LNPs. In addition to the tracking of LNPs, the AIE FL of TPE lipids can be a sensitive indicator of the LNP status because the drug loading, delivery, and release processes involve changes in lipid aggregation, which may be accompanied by the response of AIE FL. To sensitively monitor these processes with responsive AIE FL, TPE should be placed at a sensitive site and appropriately conjugated. Due to the hydrophobicity and π–π interactions of TPE, mono- and di-substituted TPE lipids prefer to self-assemble into compact "face-to-face" aggregates,[11] resulting in always "on" AIE FL with sluggish responsiveness to local environments. In contrast, tetra-substituted TPE lipids with four amphiphilic side chains on the terminal phenyl groups may form less compact "side-by-side" aggregates due to the steric hindrance and thus sensitively report the internal and external perturbation of LNPs with AIE FL. Although some tetra-substituted TPE lipids with four hydrophilic side chains, *e.g.*, oligoethylene glycols, have recently been developed,[12] their structures and "face-to-face" aggregation behavior are very different from those of lipids. Thus, novel tetra-amphiphilic side-chain-substituted TPE lipids can provide smart LNPs with a FL tracer and a status reporter, while the novel structure, AIE FL, and aggregation mechanism can shed new light on AIE biomaterials.

Herein, we have unprecedentedly developed readily accessible TPE lipids **1**–**3** with a symmetrical tetra-substituted TPE core and 4 amphiphilic side chains for the formulation of stable, image-traceable, and stimuli-responsive PEGylated LNPs for drug delivery, and discovered the critical influence of the amphiphilic side chains on AIE FL, aggregation mode, cell membrane interaction, uptake, and cytotoxicity (Fig. 1a). Interestingly, the molecular shape of lipids **1**–**3** exactly resembles a moon jellyfish in which the M-PEGylated TPE and alkyl chains represent the bell and tentacles, respectively, while the fluorescent TPE perfectly represents the glowing 4-blade core (Fig. 1b). Hydrophilic TPE **4** with 4 monodisperse undecaethylene glycol side chains, which has a structure representative of known tetra-substituted TPE lipids,[12] is used as a control. In the lipids, the TPE core played multiple roles as a fluorescent tracer, a status reporter, and a dendritic scaffold. Multiple M-PEGs were chosen as the hydrophilic head of the lipids and branched PEGylation agents for LPNs to improve pharmacokinetics and enable thermal responsiveness. To optimize the physicochemical and biological properties of the TPE lipids, either linear long M-PEGs or branched short M-PEGs with a similar number of ethylene glycol units were used as the hydrophilic head. Meanwhile, multiple alkyl chains, either long *n*-dodecyl groups or short *n*-hexyl groups, are selected as the hydrophobic tail to initiate aggregation and encapsulate the payload. The Janus dendritic molecular structure of lipids **1**–**3** may facilitate intramolecular aggregation of the alkyl chains even at low concentrations in water, leaving the TPE moiety at the hydrophilic–hydrophobic interface, which restricts the intramolecular movements of TPE for AIE FL (Fig. 1c). Notably, compared to hydrophilic TPE **4**, the multiple M-PEGs and alkyl side chains pose a significant steric hindrance to "face-to-face" aggregation from either the hydrophilic M-PEG side or the hydrophobic alkyl group side, thus promoting "side-by-side" aggregation (Fig. 1c and d).

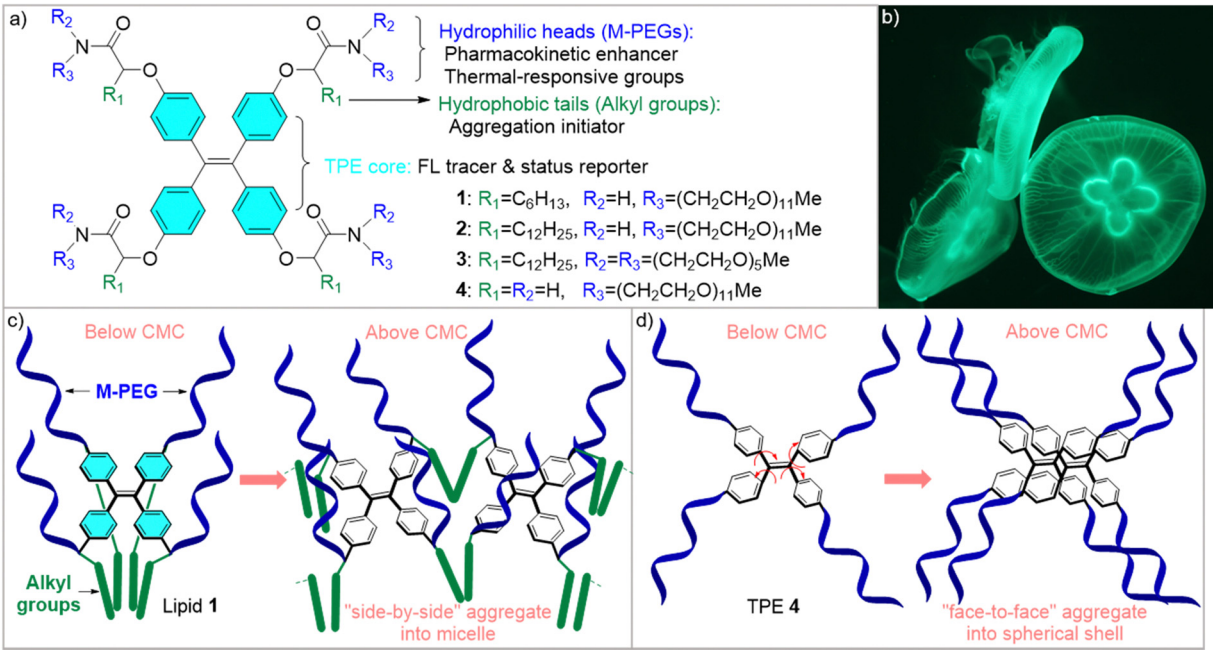

Fig. 1 Structures of TPE lipids **1**–**3** and hydrophilic TPE **4** (a). An image of the jellyfish representing the molecular structures of lipids **1**–**3** (b). The proposed mode of aggregation for lipids **1**–**3** (c) and TPE **4** (d).

Above their critical micelle concentration (CMC), lipids **1**–**3** can "side-by-side" aggregate into spherical nanoparticles with a PEGylated surface, a hydrophobic alkyl core, and a fluorescent TPE interface, in which AIE FL can sensitively monitor the perturbation from the inside and outside of the LNPs.

Experimental section

General information

Triethylene glycol monomethyl ether was purchased from TCI (>98%). Pentaethylene glycol monomethyl ether was purchased from Adamas (98%). Tetrakis(4-hydroxyphenyl)ethylene was purchased from Bidepharm (98%). Unless otherwise indicated, all reagents were obtained from commercial suppliers and used without prior purification. Column flash chromatography was performed on a silica gel (200–300 mesh) with the eluent as indicated in the procedures. ^{1}H and ^{13}C NMR spectra were recorded using a Bruker 400 or 500 MHz spectrometer. Chemical shifts are in ppm and coupling constants (J) are in Hertz (Hz). ^{1}H NMR spectra were referenced to tetramethylsilane (d, 0.00 ppm) using chloroform-*d* or methanol-d_4 as a solvent, and ^{13}C NMR spectra were referenced to solvent carbons (77.16 ppm for chloroform-d or 49.86 ppm for methanol-d_4). The splitting patterns for ^{1}H NMR spectra are denoted as follows: s (singlet), d (doublet), t (triplet), q (quartet), m (multiplet), and combinations thereof. MALDI-TOF mass spectra were recorded using a Bruker Ultraflex III TOF/TOF spectrometer.

TPE lipid 1

Under an atmosphere of N_2, acid **10** (see the ESI,† 0.50 g, 0.52 mmol), 1-hydroxybenzotriazole (0.42 g, 3.12 mmol) and *N*,*N*′-diisopropylcarbodiimide (0.39 g, 3.12 mmol) were dissolved in DMF (20 mL) and stirred at room temperature for 30 min. Then, a solution of compound **12** (1.61 g, 3.12 mmol) in 30 mL of DMF was added to the mixture, and the resulting reaction mixture was stirred at 40 °C overnight. The reaction was quenched with water and extracted with EtOAc three times. The combined organic layers were dried over anhydrous Na_2SO_4, filtered, and concentrated under vacuum, and the residue was purified by flash column chromatography on the silica gel with MeOH/DCM (1/25) as eluents to give **TPE lipid 1** as a yellow-green oil (1.30 g, 84% yield). ^{1}H NMR (500 MHz, chloroform-d) δ 6.83 (d, J = 8.0 Hz, 8H), 6.80–6.74 (m, 4H), 6.58 (d, J = 7.9 Hz, 8H), 4.41 (s, 4H), 3.66–3.57 (s, 136H), 3.54 (s, 9H), 3.49 (d, J = 17.0 Hz, 24H), 3.34 (s, 14H), 1.83 (s, 8H), 1.24 (s, 32H), 0.83 (s, 12H). ^{13}C NMR (126 MHz, chloroform-d) δ 171.7, 156.0, 137.6, 132.6, 114.79, 114.77, 71.9, 70.6, 70.53, 70.48, 70.2, 69.8, 59.0, 38.7, 33.0, 31.6, 29.0, 24.8, 22.5, 14.0. MS(MALDI-TOF) m/z: $[M + Na]^+$ calcd for $C_{150}H_{264}N_4NaO_{52}^+$ 2976.8029; found 2977.8447.

TPE lipid 2 was prepared as a yellow oil (1.40 g, 98% yield) from acid **11** and compound **12** according to the synthetic procedure for compound **TPE lipid 1**. ^{1}H NMR (500 MHz, chloroform-d) δ 6.79 (d, J = 8.4 Hz, 8H), 6.72 (t, J = 5.7 Hz, 4H), 6.54 (d, J = 8.4 Hz, 8H), 4.36 (t, J = 5.7 Hz, 4H), 3.66–3.57 (m, 136H), 3.51–3.48 (m, 8H), 3.50–3.42 (m, 26H), 3.30 (s, 15H), 1.81–1.75 (m, 8H), 1.26–1.13 (m, 76H), 0.80 (t, J = 6.8 Hz, 12H). ^{13}C NMR (126 MHz, Chloroform-d) δ 171.6, 155.9, 137.5, 132.6, 114.8, 71.9, 70.54, 70.51, 70.4, 70.2, 69.7, 58.9, 53.5, 38.7, 33.0, 31.8, 29.61, 29.58, 29.5, 29.40, 29.37, 29.3, 24.9, 22.6, 14.1. MS(MALDI-TOF) m/z: $[M + Na]^+$ calcd for $C_{174}H_{312}N_4NaO_{52}^+$ 3313.1785; found 3313.0674.

TPE lipid 3 was prepared as a yellow oil (1.30 g, 93% yield) from acid **11** and compound **13** according to the synthetic procedure for compound **TPE lipid 1**. ^{1}H NMR (500 MHz, chloroform-d) δ 6.79 (d, J = 8.2 Hz, 8H), 6.56 (d, J = 8.3 Hz, 8H), 4.75 (t, J = 6.3 Hz, 3H), 3.67–3.47 (m, 161H), 3.35 (s, 24H), 1.87–1.80 (m, 9H), 1.55–1.47 (m, 4H), 1.41–1.35 (m, 5H), 1.23 (s, 80H), 0.86 (t, J = 6.8 Hz, 15H). ^{13}C NMR (126 MHz, chloroform-d) δ 156.3, 137.2, 132.5, 114.4, 71.9, 70.59, 70.56, 70.54, 70.51, 70.3, 69.2, 68.9, 59.0, 47.9, 32.6, 31.9, 29.70, 29.67, 29.62, 29.59, 29.4, 25.8, 22.7, 14.1. MS(MALDI-TOF) m/z: $[M + Na]^+$ calcd for $C_{170}H_{304}N_4NaO_{48}^+$ 3193.1362; found 3192.5923.

TPE 4 was prepared as a yellow oil (1.90 g, 82% yield) from acid **15** and compound **12** according to the synthetic procedure for compound **TPE lipid 1**. ^{1}H NMR (500 MHz, chloroform-d) δ 7.00 (t, J = 5.8 Hz, 4H), 6.94–6.82 (m, 8H), 6.67–6.54 (m, 8H), 4.37 (s, 8H), 3.66–3.51 (m, 160H), 3.51–3.41 (m, 16H), 3.32 (s, 12H). ^{13}C NMR (126 MHz, chloroform-d) δ 168.1, 155.7, 137.6, 132.6, 114.0, 71.9, 70.6, 70.52, 70.47, 70.3, 69.7, 67.2, 59.0, 38.8. MS (MALDI-TOF) m/z: $[M + Na]^+$ calcd for $C_{126}H_{216}N_4NaO_{52}^+$ 2640.427; found 2640.549.

CMC measurements

CMC measurements were performed using the Nile Red method.[17] Briefly, a stock solution of Nile Red at a concentration of 500 μM was prepared in acetone. Then 20 μL of the stock solution was added to a brown bottle (10 mL), which was allowed to evaporate the acetone in the dark. 1.0 mL of the sample solutions of various concentrations (512, 384, 256, 192, 128, 96, 64, 48, 32, 24, 12, 10, 6, 4, 2, and 1 μM) were added into these brown bottles and allowed to age overnight. The emission spectra were acquired using a Fluorolog spectrofluorometer (HORIBA, Fluoromax-4) with an excitation wavelength of 550 nm. The intensity ratios at 635 nm to those at 660 nm of various solutions were calculated and plotted against the concentrations.

Preparation of nanoparticles NP1–NP4

Take the preparation of nanoparticles **NP1** as an example. 3.0 mg of lipid **3**, 1.0 mg of medium-chain triglyceride (MCT oil), and 1.0 mg of TAM were dissolved in 1 mL of DCM. The removal of DCM under vacuum provided a thin lipid film, and then 1 mL of deionized H_2O was added. The resulting dispersion was ultrasonicated for 20 min, and nanoparticles **NP1** were collected by filtration through a 0.45-μm polycarbonate membrane.

Results and discussion

With these ideas in mind, we synthesized TPE lipids **1**–**3** and hydrophilic TPE **4** from tetraphenolethene **5** (Scheme 1), which

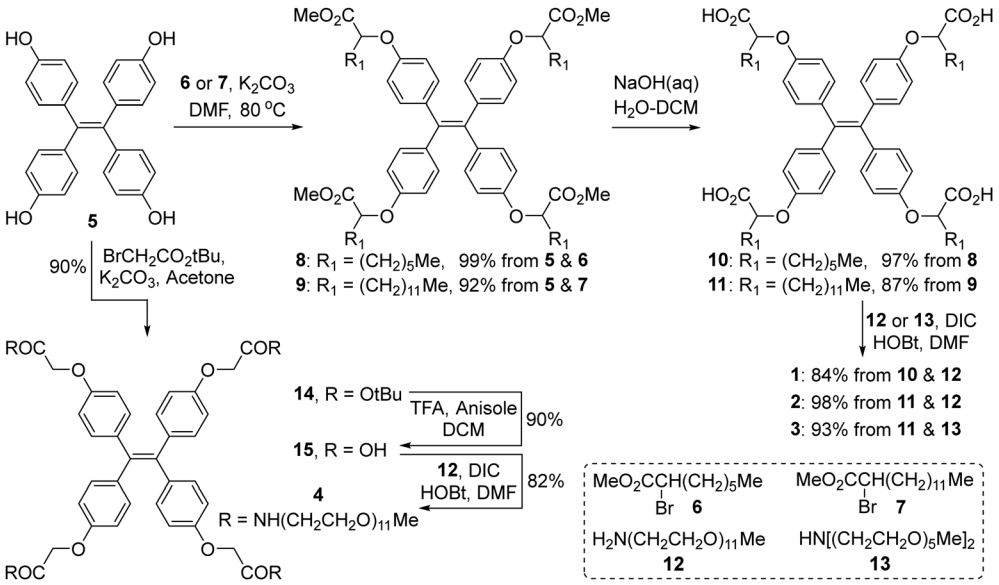

Scheme 1 Synthesis of TPE lipids **1–3** and hydrophilic TPE **4**.

was prepared using a published method.[13] First, the synthesis of lipids **1–3** was initiated by tetra-alkylation of tetraphenolethene **5** with methyl 2-bromooctanoate **6** or methyl 2-bromotetradecanoate **7** in the presence of potassium carbonate to give tetra-esters **8** and **9** in high yields. After hydrolysis of the tetra-esters with sodium hydroxide, the resulting tetra-acids **10** and **11** were then coupled with M-PEG amines **12** and **13**, prepared according to our previous protocols,[14] to give lipids **1–3**. The three-step synthesis is highly efficient and scalable, providing lipids **1–3** on multi-hundred-milligram scales with overall yields of 74% to 81%. Second, the synthesis of hydrophilic TPE **4** was initiated by tetra-alkylation of phenol **5** with *tert*-butyl 2-bromoacetate using potassium carbonate as the base, which afforded tetra-ester **14** in high yield. After the removal of the *tert*-butyl protecting groups in tetra-ester **14** with trifluoroacetic acid, the resulting tetra-acid **15** was coupled with M-PEG amine **12** to afford TPE **4** on a multi-hundred-milligram scale in 66% yield over 3 steps. The monodisperse structures of lipids **1–3** and TPE **4** were confirmed using their $^{1}H/^{13}C$ NMR and Maldi-Tof mass spectra (see the ESI†).

With their unprecedented jellyfish structures, the physicochemical properties of TPE lipids **1–3** were comparatively studied to reveal the structure–property relationship. First, their lipophilicity was measured by the water-octanol partition coefficient (Log *P*), which showed that TPE **4** is 138 times more hydrophilic than lipids **1–3** (Fig. 2a). Interestingly, despite the different side chains, lipids **1–3** showed very close Log *P*s around 1.49, suggesting that neither the alkyl chain length nor the arrangement of M-PEGs but the jellyfish-shaped molecular geometry plays a major role in their lipophilicity, which is quite different from regular PEGylated molecules.[8] Notably, lipids **1–3** and TPE **4** have good water solubilities of above 10 g L^{-1} due to the multiple hydrophilic M-PEGs. Second, TPE **4** gave intense ultraviolet (UV) absorption peaks at 254 nm and 315 nm in water, while lipids **1** and **2** gave slightly red-shifted absorption peaks at 258 nm and 328 nm, and lipid **3** gave even more red-shifted absorption peaks at 260 nm and 334 nm (Fig. 2b). The redshifts indicated that the amphiphilic side chains significantly modulate the conformation of the TPE core in lipids **1–3**. Furthermore, measurements of the molar extinction coefficient (ε) showed that the introduction of alkyl side chains significantly increased the photon absorption by up to 1.6-fold, whereas the replacement of long linear PEGs with branched short ones significantly decreased the photon absorption (Fig. 2c). Third, when the solvent was changed from methanol to water, lipids **1–3** gave red-shifted UV absorption peaks (Fig. S1, ESI†) and enhanced FL emission peaks around 490 nm (Fig. 2d–f). The enhancement of FL intensity of up to 19-fold is visible to the naked eye (inset photographs in Fig. 2d–f), illustrating their strong AIE capability. In contrast, TPE **4** emitted negligible FL during the process (Fig. 2g), indicating its low aggregation tendency and AIE capability. Compared to TPE **4**, lipids **1–3** had up to 21-fold higher FL quantum yields in water (Fig. 2h). Finally, the thermal sensitivity of lipids **1–3** was investigated using the LCST measurements. When the temperature was increased, the turbidity curves showed sharp LCSTs of 66.5 °C, 71.6 °C, and 43.6 °C for lipids **1**, **2**, and **3**, respectively (Fig. 2i and Fig. S2, ESI†), indicating that it is not the length of the alkyl chains (lipid **1** *versus* lipid **2**), but the arrangement of the M-PEGs (lipid **2** *versus* lipid **3**) that dominates the LCST. Compared to the blunt LCSTs of regular PEGylated materials,[15] the sharp LCSTs of lipids **1–3** are a result of precise molecular structures. Notably, the efficient tuning of the LCST from 71.6 °C of lipid **1** to 43.6 °C of lipid **3** with branched M-PEGs demonstrated a valuable strategy for the construction of thermo-responsive materials. In contrast, no LCST was found for TPE **4** in the temperature range. These results show that the hydrophobic alkyl side chains in lipids **1–3** promote lipophilicity and aggregation, the M-PEG side chains provide high

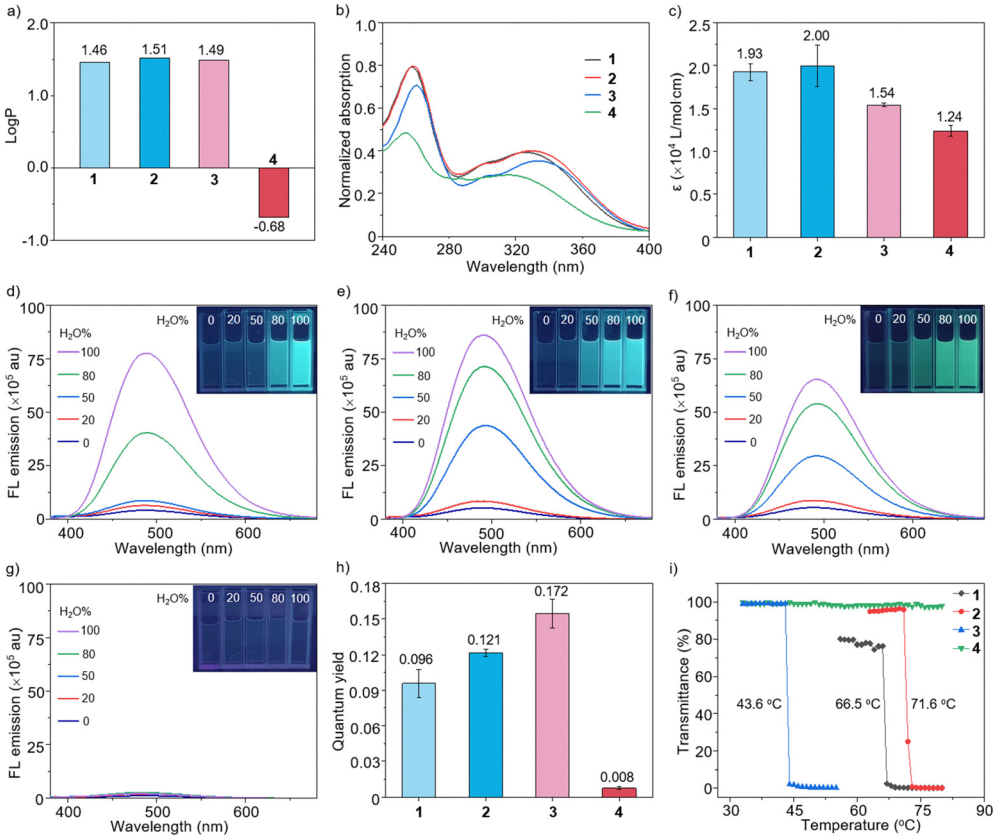

Fig. 2 Log *P* (a), UV absorption spectra (b), molar extinction coefficients (c), solvent-dependent FL emission spectra with the inset photographs of solutions under 365 nm UV excitation (d): **1**, (e): **2**, (f): **3**, and (g): **4**, solvent changed from methanol to water, $\lambda_{exciting}$ = 340 nm, FL quantum yield (h), and turbidity curves for LCST measurements (i) of TPE lipids **1**–**3** and hydrophilic TPE **4**. The concentrations for UV, FL, and LCST measurements were at 31 μM, 50 μM, and 1 mM, respectively. Unless otherwise noted, the solvent was water in all cases.

water solubility and thermal responsiveness, and the TPE core sensitively reports the aggregation status with AIE FL, in which the tetra-substituted jellyfish geometry facilitates their peculiar properties. In addition, the optical properties and thermo-responsiveness can be precisely manipulated by the length and arrangement of the M-PEGs and alkyl side chains.

The peculiar physicochemical properties of TPE lipids **1**–**3** prompted us to investigate their aggregation modes in water. First, the ^{1}H NMR spectra of lipids **1**–**3** showed significant downfield shifts of the M-PEG peaks and slight upfield shifts of the alkyl peaks when switching the solvent from methanol to deuterated water (Fig. 3a–c and Fig. S3, ESI†), indicating the hydrophilic environment of the M-PEG and the hydrophobic environment of the alkyl groups in deuterated water. Meanwhile, the complicated shifts of the aromatic peaks indicated that the TPE core was probably located at the hydrophilic–hydrophobic interface. The significant ^{1}H NMR peak broadening of lipids **1**–**3** suggested the formation of aggregates in deuterated water.[16] In contrast, the negligible line broadening of aromatic peaks in TPE **4** showed its low aggregation tendency, while the significant downfield shifts indicated the formation of π–π interactions among the TPE lipids (Fig. S3, ESI†). Second, using Nile Red as an FL probe,[17] the CMCs of lipids **1**–**3** were measured to be 41.7 μM, 22.3 μM, and 28.3 μM, respectively, demonstrating that the alkyl chain length (lipid **1** *versus* lipid **2**) rather than the M-PEG geometry (lipid **2** *versus* lipid **3**) plays a major role in their aggregation tendency (Fig. 3d). In contrast, hydrophilic TPE **4** showed a significantly higher CMC of 86.7 μM (Fig. 3d). Third, the concentration-dependent AIE FL of lipids **1**–**3** was used to monitor the aggregation. When the intensities of the maximum FL emissions at 488 nm were plotted against the concentrations, three FL response states were unexpectedly found from the TPE lipids (Fig. 3e), *i.e.*, an intensity abrupt increase state (S_1), an intensity steady increase state (S_2), and an intensity decrease state (S_3), showing that their AIE FL efficacy decreased with the concentrations. Since most AIE molecules (AIEgens) usually emit higher AIE FL at higher concentrations, lipids **1**–**3** probably have quite different modes of AIE FL. Furthermore, the almost identical transition concentrations between the states of lipids **1**–**3** suggested that neither the alkyl chain length nor the PEG arrangement but the jellyfish-shaped molecular geometry dominates their concentration-dependent AIE FL. In contrast, TPE **4** emitted negligible FL across the concentrations (Fig. 3e). Finally, dynamic light scattering (DLS) and transmission electron microscopy (TEM) were used to examine the aggregates of lipids **1**–**3** at three concentrations (5 μM, 100 μM, and 1000 μM, corresponding to the three FL response states). DLS showed

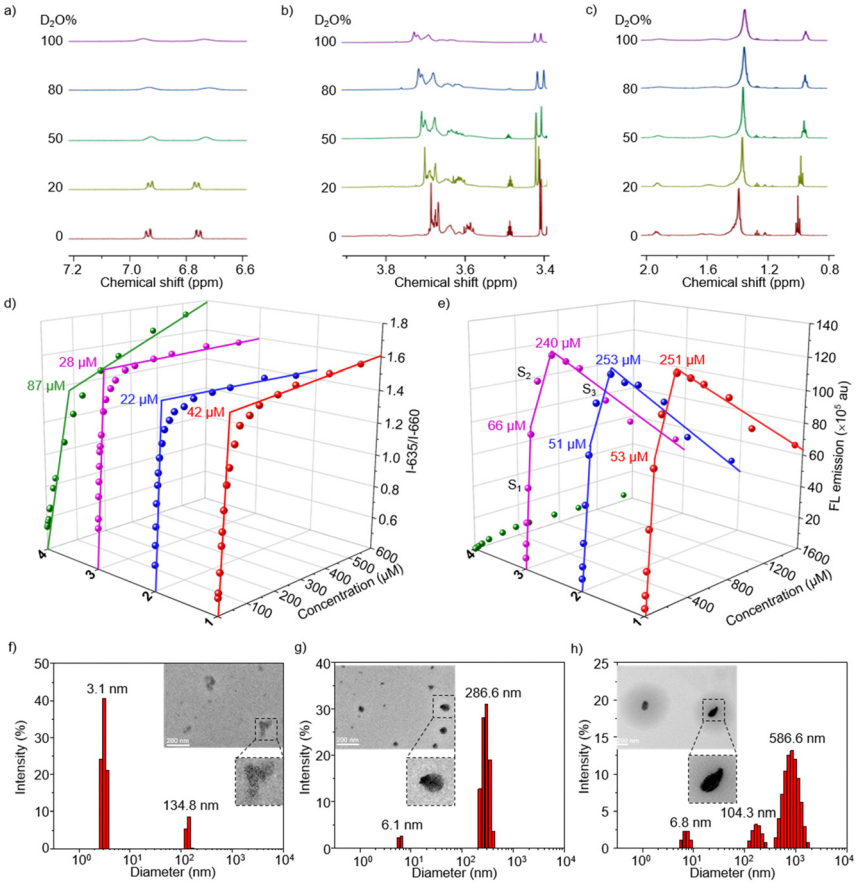

Fig. 3 The partial ^{1}H NMR spectra of TPE lipid **3** ((a): aromatic protons, (b): M-PEG protons, and (c): alkyl protons, when the solvent was changed from deuterated methanol to deuterium oxide at 50 μM). The plot of Nile Red FL intensity ratios of 635 nm to 660 nm *versus* concentrations of lipids **1**–**3** and TPE **4** (d). The plot of maximum FL intensity *versus* TPE concentration of lipids **1**–**3** and TPE **4** (e). DLS with the inset TEM images of lipid **3** ((f): 5 μM, (g): 100 μM, and (h): 1000 μM). The corresponding DLS and TEM images of lipids **1**, **2**, and TPE **4** are included in the ESI.†

that lipids **1**–**3** aggregated into very heterogeneous particles in the S_1 state (Fig. 3f and Fig. S4, ESI†) and more homogeneous particles around 350 nm in S_2 (Fig. 3g and Fig. S4, ESI†) and S_3 states (Fig. 3h and Fig. S4, ESI†).

From the TEM images, it was found that lipids **1**–**3** aggregate into large particles of loosely tangled tiny small particles in S_1 states, more tightly tangled particles in S_2 states, and compact particles in S_3 states, while TPE **4** aggregates into spherical micelles across the concentrations (inset images in Fig. 3f–h and Fig. S4, ESI†). Therefore, the aggregation of lipids **1**–**3** and TPE **4** was investigated in terms of the local environment of the alkyl groups, the M-PEGs, and the TPE core by ^{1}H NMR, the formation of hydrophobic compartments for the hydrophobic guests Nile Red by CMC measurements, the AIE FL of the TPE core by concentration-dependent AIE FL, and the morphology of the aggregates by DLS and TEM, which provided comprehensive information to understand their aggregation modes.

To better understand their aggregation in water, molecular dynamics simulations were performed on lipids **1**–**3** and TPE **4**. First, the stable conformations of lipids **1**–**3** were simulated, in which the TPE core was wrapped up by the alkyl chains with the M-PEG chains randomly looped around (Fig. 4a). Compared to TPE **4**, the alky chains in lipids **1**–**3** posed a significant steric hindrance to ''face-to-face'' aggregation. Second, the root mean square deviations (RMSDs) of the aromatic groups in lipids **1**–**3** and TPE **4** were simulated in a time range of 200 ns to evaluate the intramolecular motion of the TPE core (Fig. S5, ESI†). The highest frequency of conformational changes of the TPE core was found in TPE **4**, followed by lipids **3**, **1**, and **2** (Fig. 4b), indicating that the alkyl chains significantly restricted the movement of the TPE core, probably by aggregating into a hydrophobic core as shown by ^{1}H NMR. It was found that the short *n*-hexyl groups were not as efficient in aggregating into a hydrophobic core as the long *n*-octyl groups (lipid **1** *versus* lipid **2**), while the branched M-PEGs were not as efficient in stabilizing the TPE as the linear M-PEGs (lipid **2** *versus* lipid **3**). Third, the dihedral angle (θ) of the two *trans*-aromatic groups was simulated to evaluate the stability of the possible monomolecular micelles. The changes in the dihedral angle ($\Delta\theta$) in 1 ns showed the largest changes of 135 for TPE **4**, while dramatically smaller changes of less than 60 for lipids **1**–**3** (Fig. 4c), suggesting that lipids **1**–**3** can form quite stable monomolecular micelles, especially lipid **2** with long *n*-octyl and linear M-PEG side chains. Finally, the aggregation of the alkyl side chains was simulated to further reveal the tendency of hydrophobic effect-driven aggregation. It was found that the long *n*-dodecyl groups

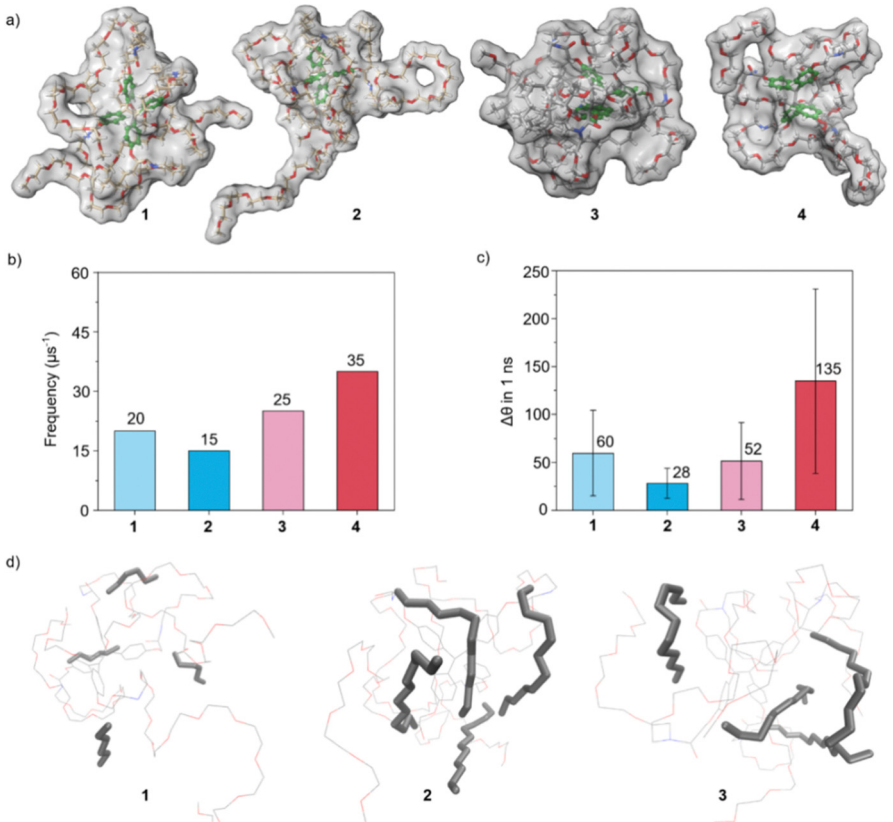

Fig. 4 Molecular dynamics simulated stable conformations in water (a), frequency of TPE core conformational changes with an average RMSD of >3.5 Å (b), changes of the two trans-aromatic group dihedral angles $\Delta\theta$ for 1 ns (c) in lipids **1**–**3** and TPE **4**, and the aggregation of the alkyl side chains in lipids **1**–**3** (The bold ones are alkyl side chains and the light ones are M-PEG side chains) (d).

in lipid **2** had a much higher tendency to aggregate intramolecularly than the short *n*-hexyl groups in lipid **1**, while the branched M-PEGs in lipid **3** somewhat alleviated the aggregation of the *n*-dodecyl side chains (Fig. 4d). Therefore, the dynamics simulations showed that the long *n*-dodecyl side chains and linear M-PEGs promoted intramolecular aggregation and provided stable monomolecular micelles with the restricted intramolecular motion of the TPE core for high AIE efficacy, which was in good agreement with the experimental data of AIE FL, DLS, and TEM.

Tetra-substituted hydrophilic TPEs, such as TPE **4**, have been reported to aggregate "face-to-face" into spherical shells,[12] which was confirmed using the ^{1}H NMR spectrum and the spherical nanoparticles in the TEM images of TPE **4** (Fig. S4, ESI†). However, the sharp aromatic proton peaks and the molecular dynamics simulation results showed that the nanoparticles are quite fragile. In contrast, the ^{1}H NMR, CMC, FL, DLS, and TEM results of lipids **1**–**3** showed quite different aggregation modes. Although the alky side chains in lipids **1**–**3** promoted intramolecular aggregation into monomolecular micelles, the resulting Janus dendritic structures pose a significant steric hindrance to "face-to-face" aggregation and promote "side-by-side" aggregation, as indicated by the molecular dynamics simulations. 2D ROESY experiments were additionally conducted to detect the ^{1}H–^{1}H through-space contacts of TPE lipids. Stronger correlations were observed between the TPE cores, and the M-PEG and TPE core of TPE **4** when changing the solvent from methanol to water (Fig. S6, ESI†), owing to the "face-to-face" aggregation in water. However, except for the correlation between the alkyl group and M-PEGs, no significant correlation between the TPE cores was observed in the ROESY spectra of lipid **3** (Fig. S6, ESI†), indicating that the amphiphilic side chains restricted the intramolecular motion of the TPE cores and the "face-to-face" aggregation. Moreover, the significantly higher FL emissions of lipids **1**–**3** than that of TPE **4** over the concentration range from 3.9 μM to 1500 μM (Fig. 3e), as well as the upfield shifts of the alkyl peaks in their ^{1}H NMR spectra (Fig. 3a–c and Fig. S3, ESI†), further suggest that the intramolecular motion of the TPE cores is always restricted by the amphiphilic side chains. Based on the above results, we proposed the concentration-dependent aggregation of lipids **1**–**3**. Below the CMCs, lipids **1**–**3** tend to self-assemble into monomolecular micelles with an efficiently restricted intramolecular motion of the TPE core, which leads to high AIE FL efficacy and thus the FL intensity increases abruptly with concentration in the S_1 state (Fig. 3e and Fig. S4, ESI†). Due to the entanglement of the M-PEGs, the monomolecular micelles would randomly form loose aggregates as detected by DLS and TEM (Fig. 3f and Fig. S4, ESI†). Above the CMCs, the monomolecular micelles of lipids **1**–**3** aggregate "side-by-side" into homogeneous nanoparticles as

detected by DLS and TEM (Fig. 3g and Fig. S4, ESI†), in which the alkyl chains may intermolecularly tangle, reducing the efficiency of AIE, and thus the FL intensity steadily increases with the concentration in the S_2 states (Fig. 3e and Fig. S4, ESI†). In the S_3 states of high concentrations, the nanoparticles of lipids **1**–**3** are further fused into large compact micelles (Fig. 3h and Fig. S4, ESI†), in which the lipid molecules inside the micelles are randomly entangled and the AIE efficiency is further degraded, resulting in a decrease in FL. Meanwhile, the inner filter effect (IFE)[18] also plays an important role in reducing the FL intensity at high concentrations (Fig. 3e). Despite the differences in the length of the alkyl groups and the geometry of the M-PEGs, lipids **1**–**3** exhibited similar aggregation behaviors, indicating that the peculiar concentration-dependent aggregation is mainly caused by their jellyfish-shaped molecular geometry. Therefore, lipids **1**–**3** tend to aggregate "side-by-side" in water above the CMC like regular phospholipids, while the FL sensitively reports the transitions of aggregation states, enabling them as novel FL-traceable smart lipids.

With the preferred AIE FL and aggregation modes, the biocompatibility, cell uptake, and biosafety of lipids **1**–**3** were then investigated in cells. Surprisingly, a structure-dependent biocompatibility profile of lipids **1**–**3** was identified in human lung cancer A549 cells, human breast cancer MCF-7 cells, and normal human breast MCF-10A cells (Fig. 5a–c and Table S1, ESI†). Lipid **1** with short *n*-hexyl side chains showed significant cytotoxicities against all cells, whose half-maximal inhibitory concentration (IC_{50}) was calculated experimentally from 19.1 to 35.2 μM. Lipid **2** with long *n*-dodecyl side chains showed dramatically improved biocompatibility, and lipid **3** with *n*-dodecyl and branched M-PEG side chains showed no apparent cytotoxicity (IC_{50} > 100 μM). In comparison, TPE **4** without alkyl side chains showed high biocompatibility towards all cells. Obviously, long alkyl and branched M-PEG side chains in the lipids promote high biocompatibility. Next, confocal microscopy images were used to compare the uptake of lipids **1**–**3** and TPE **4** in MCF-7 cells (Fig. 5d and Fig. S7a, ESI†). Using DiI as a cell membrane dye, lipid **1** showed a significantly higher uptake than lipids **2** and **3**, while TPE **4** showed a negligible uptake. These observations suggest that the high cytotoxicity of lipid **1** is probably related to the low stability of the aggregates, as shown in molecular dynamics simulations, where the short *n*-hexyl side chains in the aggregates are prone to reassembly, interaction with cell membranes, and thus high uptake by cells. In contrast, the long *n*-dodecyl side chains in lipid **2** are tightly aggregated as indicated by molecular dynamics simulations, difficult to reassemble and interact with cell membranes, leading to lower cell uptake and cytotoxicity. PEGylation is a well-established strategy to improve pharmacokinetics and biocompatibility while reducing cell uptake.[4] Lipid **3** aggregates are better PEGylated by the branched M-PEGs, resulting in even lower cell uptake. Our results showed that the introduction of short alkyl groups into PEGylated molecules, such as TPE **4**, can significantly promote cell uptake and induce cytotoxicity, which may be of great value for the rational design of PEGylated drugs. Finally, the biosafety of lipids **1**–**3** and TPE **4** was evaluated by the hemolysis assay. Fortunately, no obvious hemolysis (<5%) of these compounds was found at a concentration of up to 160 μM (Fig. 5e and Fig. S8, ESI†). Although the origin of the cytotoxicity of lipid **1** is not clear, cell membrane disruption is not a cause of cytotoxicity as indicated by the hemolysis assay results. Therefore, as novel FL-traceable lipids, the cell membrane permeability and biocompatibility of the

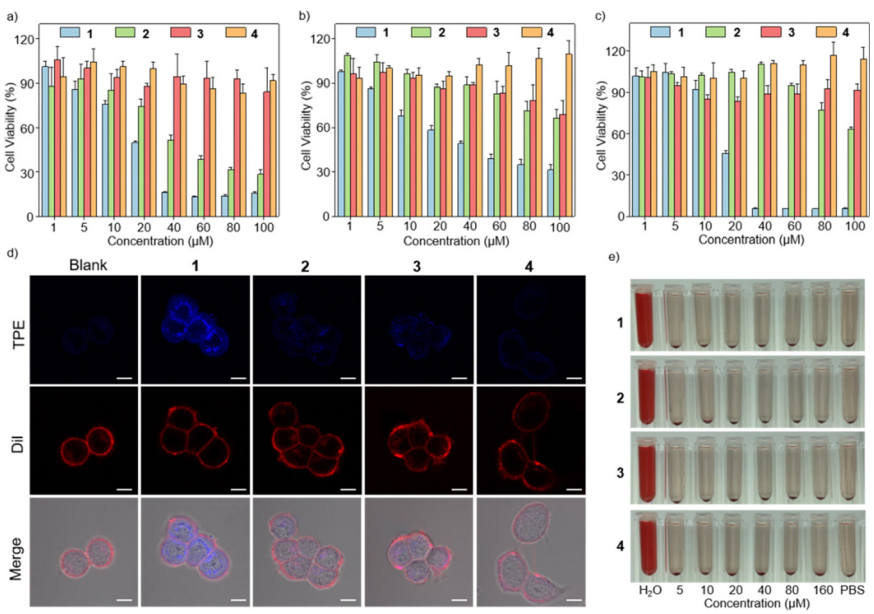

Fig. 5 Biocompatibility assay of lipids **1**–**3** and TPE **4** in A549 cells (a), MCF-7 cells (b), and MCF-10A cells (c) using the CCK-8 assay. The confocal microscopy images of MCF-7 cells after incubation with 20 μM of lipids **1**–**3** and TPE **4** for 24 hours, scale bar: 10 μm (d). Hemolysis assay of red blood cells from BALB/c mice treated with the indicated concentrations of lipids **1**–**3** and TPE **4** with water and PBS as controls (e).

TPE lipids can be conveniently optimized by the length of alkyl side chains and the arrangement of the M-PEGs, which provided lipid **3** as a promising smart lipid for the downstream study. Finally, lipid **3** was employed to formulate a clinical hormone therapy drug, tamoxifen, into nanoparticles for breast cancer therapy. First, two widely used phospholipids, HSPC and DSPE-PEG$_{2000}$, were used as comparisons to evaluate the formulation capability of lipid **3**. Medium-chain triglyceride (MCT oil), a widely used pharmaceutical ingredient for hydrophobic drug formulation, was used to dissolve tamoxifen and create a hydrophobic core for the nanoparticles. Molecular dynamics simulations revealed a structure-dependent interaction between lipids **1**–**3** and MCT oil. Lipid **1** tends to remain at the water–MCT oil interface and lipid **2** tends to dissolve in MCT oil, while lipid **3** tends to insert the *n*-dodecyl side chains into MCT oil and leave the M-PEGs in water (Fig. 6a). The biphasic profile of lipid **3** may favor its "side-by-side" assembly on the MCT droplet with high AIE FL and PEGylated nanoparticle surfaces. Indeed, with lipid **3**, MCT oil, and a tamoxifen ratio of 3 : 1 : 1, monodisperse fluorescent nanoparticles **NP1** were prepared with a particle size of 153 nm and a polydispersity index (PDI) of 0.24 (Fig. 6b). Although comparable in formulation capability to HSPC and DSPE-PEG$_{2000}$ (**NP2** and **NP3** in Fig. 6b), the multi-functions of lipid **3**, such as AIE FL and PEGylation, are highly advantageous. Second, using the same method as **NP1**, nanoparticles **NP1-1** and **NP1-2** were prepared using lipids **1** and **2**, respectively. The DLS results showed that the formulated **NP1-1** and **NP1-2** had a broad particle size distribution (Table S2, ESI†), indicating that remaining at the water–oil interface (lipid **1**) or dissolving in the oil (lipid **2**) was unfavorable to the formation of nanoparticles. Third, lipid **3** was used as a helper lipid to formulate tamoxifen-loaded smart nanoparticles. Monodisperse fluorescent nanoparticles **NP4** with a particle size of 147 nm and a PDI of 0.15 were conveniently prepared with soy phospholipid S75, lipid **3**, and tamoxifen in a ratio of 25 : 5 : 1 (Fig. 6c). In contrast, very heterogeneous nanoparticles were obtained when HSPC and DSPE-PEG$_{2000}$ were used instead (Table S3, ESI†). Nanoparticles **NP4** showed high stability in water, PBS, and the DMEM cell culture medium for 14 days (Fig. 6d). A high drug loading content of 4.9% and a drug encapsulation efficiency of 96% could be obtained for nanoparticles **NP4** (Table S4, ESI†). The drug release study revealed that tamoxifen was released from **NP4** with a slow release rate, and the maximum percentage of tamoxifen release was 39% after 72 h, which is similar to the control nanoparticles (F68@TAM). In addition, an acid-promoted tamoxifen release was observed from **NP4**, probably due to the protonation of tamoxifen at pH 5.5 (Fig. 6e). Finally, the biocompatibility and cytotoxicity of nanoparticles **NP4** were evaluated. Compared to tamoxifen, nanoparticles **NP4** showed significantly higher biocompatibility in MCF-10A cells (IC_{50}: 46.2 μM *vs.* 29.5 μM) and dramatically improved cytotoxicity in MCF-7 cells (IC_{50}: 10.1 μM *vs.* 20.2 μM) (Fig. 6f and Fig. S9, Table S5, ESI†). With the AIE FL of lipid **3**, confocal microscopy images showed that nanoparticles **NP4** were efficiently taken up by MCF-7 cells (Fig. 6g and Fig. S7b, ESI†), indicating that

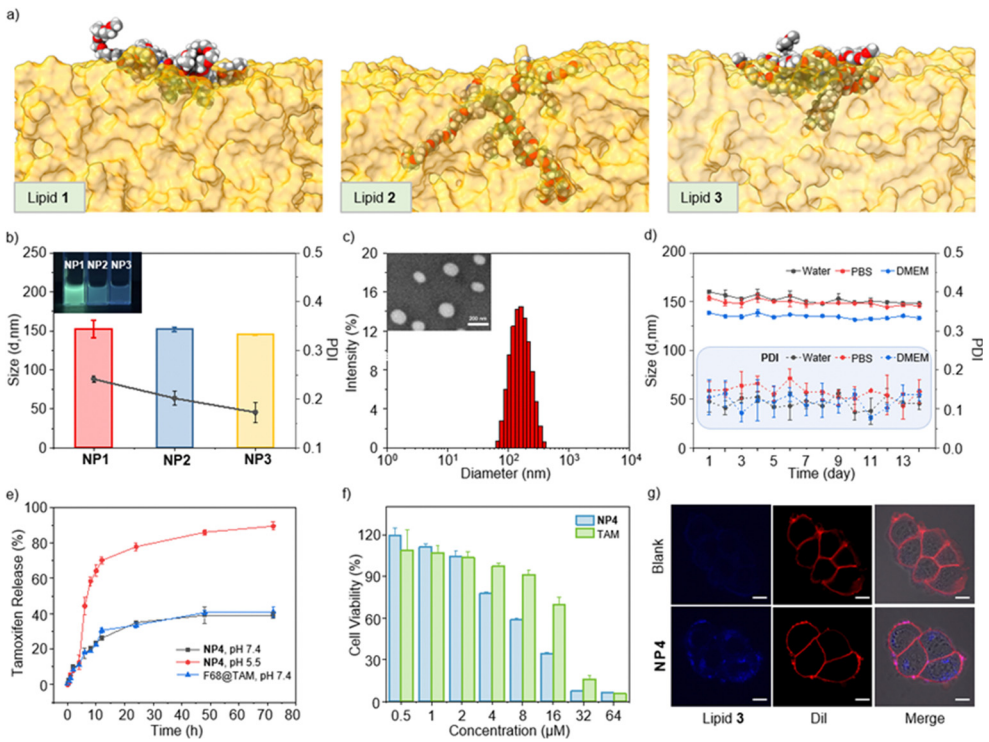

Fig. 6 Molecular dynamics simulated interactions of lipids **1**–**3** with MCT oil (a), size and PDI of nanoparticles **NP1**–**NP3** with the inset photographs of nanoparticles under 365 nm UV excitation (b). DLS with the inset TEM images (c), 14-day stability in different media over (d), tamoxifen release curve (e), cytotoxicity assay (f) and confocal microscopy images (g) in MCF-7 cells of nanoparticles **NP4**, scale bar: 10 μm.

lipid **3**, as a helper lipid, can PEGylate the nanoparticle without hindering cell uptake. Therefore, lipid **3** can efficiently formulate therapeutic drugs like a phospholipid and provide monodisperse, stable, fluorescent, thermal-responsive, and biocompatible PEGylated smart nanoparticles.

Conclusions

In summary, inspired by the glowing dendritic structure of the moon jellyfish, we have developed a series of readily available tetra-substituted TPE lipids with four amphiphilic side chains to mimic the structure of jellyfish as unprecedented multifunctional smart lipids for the convenient preparation of nanoparticles with PEGylated surfaces, and real-time FL monitoring of drug uptake. The convenient 3-step synthesis enables the rapid preparation of the TPE lipids on the multi-hundred-milligram scale with high efficiency. Through physicochemical property studies, we discovered the unique jellyfish structure-dependent lipophilicity, fluorescence quantum yield, thermal responsiveness, and aggregation mode of these lipids. The structure–property relationship study and molecular dynamics simulation of the lipids show intramolecular aggregation into unimolecular micelles below the CMC and "side-by-side" aggregation like phospholipids into nanoparticles above the CMC. The peculiar aggregation mode of the lipids not only provides a novel AIE mechanism but also sensitive fluorescence to monitor the aggregation status. Importantly, it was found that the balance between PEGylation and alkylation in the lipids significantly influences the stability of the aggregates, cell uptake, and biocompatibility, which would be of great importance for the design of PEGylated pharmaceuticals. Through the systematic screening of physicochemical and biological properties, a TPE lipid with *n*-dodecyl and branched M-PEG side chains, optimized LCST, and high biocompatibility was selected for the formulation of the breast cancer drug tamoxifen into smart nanoparticles. It was found that the TPE lipid can be used as the sole lipid or as a helper lipid to efficiently encapsulate tamoxifen and provide stable, monodisperse, and fluorescent smart nanoparticles for real-time fluorescence monitoring of drug uptake, and improved breast cancer therapy in cells. Through the development of these unprecedented jellyfish structure lipids, we not only discovered a hidden application of AIEgens, but also revealed novel AIE mechanisms and peculiar properties, which would be highly beneficial for the rational design and broad application of AIEgens, especially in drug delivery by the lipid-based nanoparticles. The application of the TPE lipid-based smart nanoparticles in cancer therapy in animals is under active investigation in this group.

Author contributions

The manuscript was written through contributions from all authors. All authors have approved the final version of the manuscript.

Conflicts of interest

The authors declare no competing financial interest.

Acknowledgements

This work was supported by the National Key R&D Program of China (2018YFA0704000), the National Natural Science Foundation of China (22077098, U21A20392, 21921004, and 82127802), and the Knowledge Innovation Program of Wuhan-Basic Research (2022020801010137). Shizhen Chen acknowledges the support from the Youth Innovation Promotion Association and the Young Top-notch Talent Cultivation Program of Hubei Province.

References

1 (*a*) A. Beloqui, M. Á. Solinís, A. Rodríguez-Gascón, A. J. Almeida and V. Préat, Nanostructured lipid carriers: Promising drug delivery systems for future clinics, *Nanomedicine*, 2016, **12**, 143–161; (*b*) C. Tapeinos, M. Battaglini and G. Ciofani, Advances in the design of solid lipid nanoparticles and nanostructured lipid carriers for targeting brain diseases, *J. Controlled. Release*, 2017, **264**, 306–332; (*c*) H. M. G. Barriga, M. N. Holme and M. M. Stevens, Cubosomes: The next generation of smart lipid nanoparticles?, *Angew. Chem., Int. Ed.*, 2019, **58**, 2958–2978; (*d*) M. Haider, S. M. Abdin, L. Kamal and G. Orive, Nanostructured lipid carriers for delivery of chemotherapeutics: A review, *Pharmaceutics*, 2020, **12**, 288.

2 M. D. Shin, S. Shukla, Y. H. Chung, V. Beiss, S. K. Chan, O. A. Ortega-Rivera, D. M. Wirth, A. Chen, M. Sack, J. K. Pokorski and N. F. Steinmetz, COVID-19 vaccine development and a potential nanomaterial path forward, *Nat. Nanotechnol.*, 2020, **5**, 646–655.

3 (*a*) X. C. Hou, T. Zaks, R. Langer and Y. Z. Dong, Lipid nanoparticles for mRNA delivery, *Nat. Rev. Mater.*, 2021, **6**, 1078–1094; (*b*) R. S. Riley, M. V. Kashyap, M. M. Billingsley, B. White, M.-G. Alameh, S. K. Bose, P. W. Zoltick, H. Li, R. Zhang, A. Y. Cheng, D. Weissman, W. H. Peranteau and M. J. Mitchell, Ionizable lipid nanoparticles for in utero mRNA delivery, *Sci. Adv.*, 2021, **7**, eaba1028; (*c*) T. T. H. Thi, E. J. A. Suys, J. S. Lee, D. H. Nguyen, K. D. Park and N. P. Truong, Lipid-based nanoparticles in the clinic and clinical trials: From cancer nanomedicine to COVID-19 vaccines, *Vaccines*, 2021, **9**, 359; (*d*) K. Hashiba, Y. Sato, M. Taguchi, S. Sakamoto, A. Otsu, Y. Maeda, T. Shishido, M. Murakawa, A. Okazaki and H. Harashima, Branching ionizable lipids can enhance the stability, fusogenicity, and functional delivery of mRNA, *Small Sci.*, 2022, 2200071; (*e*) H. Q. Cao, Y. Yang and J. B. Li, AIEgen-lipid structures: Assembly and biological applications, *Aggregate*, 2020, **1**, 69–79.

4 (*a*) C. Fishburn, The pharmacology of PEGylation: balancing PD with PK to generate novel therapeutics, *J. Pharm. Sci.*, 2008, **97**, 4167–4183; (*b*) D. Pozzi, V. Colapicchioni, G. Caracciolo, S. Piovesana, A. L. Capriotti, S. Palchetti, S. De Grossi, A. Riccioli, H. Amenitsch and A. Lagana, Effect of polyethyleneglycol (PEG) chain length on the bio-nano-interactions between PEGylated lipid nanoparticles and biological fluids: from nanostructure to uptake in cancer

cells, *Nanoscale*, 2014, **6**, 2782–2792; (*c*) J. S. Suk, Q. G. Xu, N. Kim, J. Hanes and L. M. Ensign, PEGylation as a strategy for improving nanoparticle-based drug and gene delivery, *Adv. Drug Delivery Rev.*, 2016, **99**, 28–51.

5 (*a*) J. E. Seely and C. W. Richey, Use of ion-exchange chromatography and hydrophobic interaction chromatography in the preparation and recovery of polyethylene glycol-linked proteins, *J. Chromatography A*, 2001, **908**, 235–241; (*b*) C. J. Fee and J. M. van Alstine, PEG-proteins: reaction engineering and separation issues, *Chem. Eng. Sci.*, 2006, **61**, 924–939; (*c*) M. J. Vicent, L. Dieudonne, R. J. Carbajo and A. Pineda-Lucena, Polymer conjugates as therapeutics: future trends, challenges and opportunities, *Expert Opin. Drug Delivery*, 2008, **5**, 593–614.

6 (*a*) Z. Q. Yu, S. W. Bo, H. Y. Wang, Y. Li, Z. G. Yang, Y. Z. Huang and Z.-X. Jiang, Application of monodisperse PEGs in pharmaceutics: monodisperse polidocanols, *Mol. Pharm.*, 2017, **14**, 3473–3479; (*b*) T. Deng, X. L. Mao, Y. Xiao, Z. G. Yang, X. Zheng and Z.-X. Jiang, Monodisperse oligoethylene glycols modified camptothecin, 10-hydroxycamptothecin and SN38 prodrugs, *Bioorg. Med. Chem. Lett.*, 2019, **29**, 581–584.

7 (*a*) S.-L. Sim, T. He, A. Tscheliessnig, M. Mueller, R. B. H. Tan and A. Jungbauer, Branched polyethylene glycol for protein precipitation, *Biotechnol. Bioeng.*, 2012, **109**, 736–746; (*b*) Y. Vugmeyster, C. A. Entrican, A. P. Joyce, R. F. Lawrence-Henderson, B. A. Leary, C. S. Mahoney, H. K. Patel, S. W. Raso, S. H. Olland, M. Hegen and X. Xu, Pharmacokinetic, biodistribution, and biophysical profiles of TNF nanobodies conjugated to linear or branched poly(ethylene glycol), *Bioconjugate Chem.*, 2012, **23**, 1452–1462.

8 (*a*) Y. Li, X. M. Wang, Y. P. Chen, Z. G. Yang and Z.-X. Jiang, Monodisperse polyethylene glycol ''brushes'' with enhanced lipophilicity, and thermo and plasma stability, *Chem. Commun.*, 2019, **55**, 1895–1898; (*b*) X. M. Wang, Y. Li, T. J. Wu, Z. G. Yang, X. Zheng, S. Z. Chen, X. Zhou and Z.-X. Jiang, Quantitatively fine-tuning the physicochemical and biological properties of peptidic polymers through monodisperse PEGylation, *Biomacromolecules*, 2020, **21**, 725–731; (*c*) J. F. Zhu, H. B. Zhang, K. X. Chen, Y. Li, Z. G. Yang, S. Z. Chen, X. Zheng, X. Zhou and Z.-X. Jiang, Peptidic monodisperse PEG "comb" as multifunctional "add-on" module for imaging-traceable and thermoresponsive theranostics, *Adv. Healthcare Mater.*, 2020, **9**, 1901331.

9 (*a*) Y. N. Hong, J. W. Y. Lam and B. Z. Tang, Aggregation-induced emission, *Chem. Soc. Rev.*, 2011, **40**, 5361–5388; (*b*) J. Mei, N. L. C. Leung, R. T. K. Kwok, J. W. Y. Lam and B. Z. Tang, Aggregation-Induced Emission: Together We Shine, United We Soar!, *Chem. Rev.*, 2015, **115**, 11718–11940; (*c*) W. Xu, D. Wang and B. Z. Tang, NIR-II AIEgens: A Win-Win Integration towards Bioapplications, *Angew. Chem., Int. Ed.*, 2021, **60**, 7476–7487; (*d*) Z. J. Zhang, M. M. Kang, H. Tan, N. Song, M. Li, P. H. Xiao, D. Y. Yan, L. P. Zhang, D. Wang and B. Z. Tang, The fast-growing field of photo-driven theranostics based on aggregation-induced emission, *Chem. Soc. Rev.*, 2022, **51**, 1983–2030.

10 (*a*) S. Dufort, L. Sancey and J.-L. Coll, Physico-chemical parameters that govern nanoparticles fate also dictate rules for their molecular evolution, *Adv. Drug Delivery Rev.*, 2012, **64**, 179–189; (*b*) J. Gilleron, W. Querbes, A. Zeigerer, A. Borodovsky, G. Marsico, U. Schubert, K. Manygoats, S. Seifert, C. Andree, M. Stöter, H. Epstein-Barash, L. Zhang, V. Koteliansky, K. Fitzgerald, E. Fava, M. Bickle, Y. Kalaidzidis, A. Akinc, M. Maier and M. Zerial, Image-based analysis of lipid nanoparticle–mediated siRNA delivery, intracellular trafficking and endosomal escape, *Nat. Biotechnol.*, 2013, **31**, 638–646; (*c*) B. R. Smith and S. S. Gambhir, Nanomaterials for in vivo imaging, *Chem. Rev.*, 2017, **117**, 901–986.

11 A.-X. Ding, Y.-D. Shi, K.-X. Zhang, W. Sun, Z.-L. Tan, Z.-L. Lu and L. He, Self-assembled aggregation-induced emission micelle (AIE micelle) as interfacial fluorescence probe for sequential recognition of Cu2+ and ATP in water, *Sens. Actuators, B*, 2018, **255**, 440–447.

12 (*a*) T. Sanji, K. Shiraishi, M. Nakamura and M. Tanaka, Fluorescence Turn-On Sensing of Lectins with Mannose-Substituted Tetraphenylethenes Based on Aggregation-Induced Emission, *Chem. – Asian J.*, 2010, **5**, 817–824; (*b*) S. Song, H.-F. Zheng, D.-M. Li, J.-H. Wang, H.-T. Feng, Z.-H. Zhu, Y.-C. Chen and Y.-S. Zheng, Monomer Emission and Aggregate Emission of TPE Derivatives in the Presence of γ-Cyclodextrin, *Org. Lett.*, 2014, **16**, 2170–2173; (*c*) T. Takeda, S. Yamamoto, M. Mitsuishi and T. Akutagawa, Thermoresponsive Amphipathic Fluorescent Organic Liquid, *J. Phys. Chem. C*, 2018, **122**, 9593–9598.

13 (*a*) X. M. Hu, Q. Chen, J. X. Wang, Q. Y. Cheng, C. G. Yan, J. Cao, Y. J. He and B. H. Han, Tetraphenylethylene-based glycoconjugate as a fluorescence ''turn-on'' sensor for cholera toxin, *Chem. – Asian J.*, 2011, **6**, 2376–2381; (*b*) J. L. Wang, S. H. Wang, Y. Q. Zhou, X. G. Wang and Y. N. He, Fast Photoinduced Large Deformation of Colloidal Spheres from a Novel 4-arm Azobenzene Compound, *ACS Appl. Mater. Interfaces*, 2015, **7**, 16889–16895.

14 H. Zhang, X. F. Li, Q. Y. Shi, Y. Li, G. Q. Xia, L. Chen, Z. G. Yang and Z.-X. Jiang, Highly efficient synthesis of monodisperse poly(ethylene glycols) and derivatives through macrocyclization of oligo(ethylene glycols), *Angew. Chem. Int. Ed.*, 2015, **54**, 3763–3767.

15 D. Schmaljohann, J. Ostwald, B. Jørgensen, M. Nitschke, D. Beyerlein and C. Werner, Thermo-responsive PNiPAAm-g-PEG films for controlled cell detachment, *Biomacromolecules*, 2003, **4**, 1733–1739.

16 J. Hjalte, S. Hossain, A. Hugerth, H. Sjögren, M. Wahlgren, P. Larsson and D. Lundberg, Aggregation Behavior of Structurally Similar Therapeutic Peptides Investigated by ^{1}H NMR and All-Atom Molecular Dynamics Simulations, *Mol. Pharm.*, 2022, **19**, 904–917.

17 M. C. A. Stuart, J. C. van de Pas and J. B. F. N. Engberts, The use of Nile Red to monitor the aggregation behavior in ternary surfactant-water-organic solvent systems, *J. Phys. Org. Chem.*, 2005, **18**, 929–934.

18 S. Chen, Y.-L. Yu and J.-H. Wang, Inner filter effect-based fluorescent sensing systems: A review, *Anal. Chim. Acta*, 2018, **999**, 13–26.